



# Study on the wear and corrosion resistance of Fe–Mo coatings on 65Mn steel ploughshares by laser cladding

Keyang Chen<sup>1</sup> · Xuefeng Yang<sup>1</sup> · Wanyang Li<sup>1</sup> · Guofeng Xia<sup>1</sup> · Shouren Wang<sup>1</sup> · Kai Wang<sup>2</sup>

Received: 17 April 2022 / Accepted: 11 July 2022 / Published online: 18 August 2022  
© The Author(s), under exclusive licence to Springer-Verlag GmbH, DE part of Springer Nature 2022

## Abstract

To improve the wear resistance and corrosion resistance of 65Mn ploughshares, Fe–Mo coatings were coated on the surface of the 65Mn steel. The microstructure, hardness, impact toughness, wear resistance, and corrosion resistance of Fe–Mo coatings were investigated. The microstructure of the coating was dense, with no obvious defects. The hardness of the coating was nearly two times higher than that of the 65Mn. The coatings show a significant increase in wear resistance with a slight reduction in impact toughness. The electrochemical self-corrosion current density was reduced by two orders of magnitude. The wear and corrosion resistance of the coating is much better than that of 65Mn matrix. Among them, the performance of Fe–15Mo coating is the best, which can better meet the application requirements of Plowshare.

**Keywords** Fe–Mo coatings · Microstructure · Impact toughness · Wear resistance

## 1 Introduction

The soil-touching parts of agricultural machinery are often in direct contact with soil and other abrasive particles in an unlubricated state, and the working environment is very harsh. The Abrasive wear between the soil-touching parts of agricultural machinery and the soil is one of the main reasons that cause the agricultural machinery to be scrapped. In addition, the soil in a ploughed field is a complex multi-phase environment consisting of solid, liquid and gaseous, which contain moisture, fertilizer residues, pesticide residues, dissolved salts, oxygen, microorganisms, weeds and other crop residues that can cause corrosion to the ploughshare. The physical shape of common plowshare is shown in Fig. 1a, b. After corrosion, the surface of plowshare interacts with abrasive particles such as soil, which will accelerate the wear rate of the plowshare, which also requires good wear and corrosion resistance on the surface of the farming contact parts, Singh et al. Kalácska et al. and Wei et al. [1–3] Analyzed the composition of soil, the types of

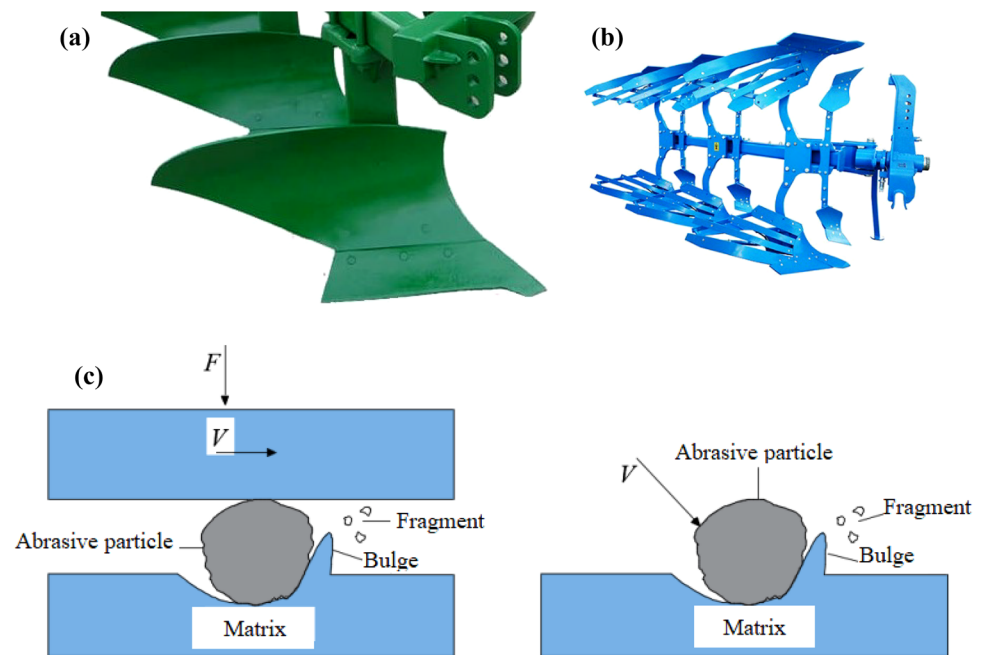
wear particles and the performance of Fe-based plowshare. The schematic diagram of Plowshare abrasive wear is shown in Fig. 1c. The adverse effect of surface problems in engineering practice is to shorten the service life of the workpiece and increase the use cost. Surface treatment technology plays a good role in solving surface problems in engineering. Coating technology and surface texture technology are typical of surface treatment technology [4–6]. Surface treatment is widely used in hard metals, non-ferrous metals and refractory metals, such as Ti-based alloy, Co-based alloy Fe-based and Mo-based alloys, and plays a key role in friction reduction, wear resistance and corrosion resistance of the surface [7–11]. Laser cladding technology has the advantage of being highly automated and easy to control compared to traditional processing methods such as thermal spraying [12]. Cheng et al. and Wen et al. [13, 14] used two laser cladding technologies to coat different high entropy alloys, analyzed the properties of alloy coatings, and showed that high entropy alloy coatings have good development prospects. The coating is uniform and dense, with few defects such as pores and cracks. Compared to Co-based and Ni-based cladding powders, Fe-based powder has similar properties with 65Mn. During the melting process, a good metallurgical bond is formed between the matrix and the coating, which has high bonding strength and low cost. These advantages make it widely used in the research and promotion of local wear-resistant parts. In recent years, Fe-based powders such

✉ Xuefeng Yang  
me\_yangxf@ujn.edu.cn

<sup>1</sup> School of Mechanical Engineering, University of Jinan, Jinan 250022, Shandong, China

<sup>2</sup> Qingdao Sufa New Material Co., Ltd, Qingdao 266109, Shandong, China

**Fig. 1** a, b Plowshare and c schematic diagram of abrasive wear



as Fe60, Fe50, Fe45, Fe35, and Fe30 have been widely studied [15, 16], More et al. [15] Discussed the effects of laser parameters, material composition and other factors on the surface quality, hardness and microstructure of the coating. Li et al. [16] found  $\text{Al}_{0.8}\text{CrFeNiCoAlCu}_x$  high entropy alloy on the coating quality shows that when  $x=0.5$ , the alloy has good bonding shear strength, good hardness, wear resistance and corrosion resistance, which is more suitable for laser modified coating on the surface of aluminum alloy but due to the difference in material ratios, problems such as low hardness and poor corrosion resistance have arisen. By summarizing the research results of different researchers, the Fe-based coating was prepared according to the actual application conditions and the actual needs of ploughshares, which performances were investigated and analyzed.

## 2 Experimental materials and methods

### 2.1 Material and sample preparation

The matrix material used in the experiment was 65Mn steel, and the heat treatment process was  $870\text{ }^\circ\text{C}\times 10\text{ min}$ ,  $180\text{ }^\circ\text{C}$  nitrate isothermal quenching and  $180\text{ }^\circ\text{C}\times 90\text{ min}$  tempering, Sun et al. [17] Found in their research that there is non tempered martensite between the heat affected zone and the cladding layer, resulting in poor plasticity and toughness of the coating. Therefore, the specimens after cladding were tempered in this experiment. The dimension of the specimens was  $50\text{ mm}\times 15\text{ mm}\times 5\text{ mm}$ . The chemical composition of 65Mn matrix is shown in Table 1.

**Table 1** Chemical composition of 65Mn matrix (wt.%)

C	Si	Mn	Ni	Cr	Fe
0.62–0.70	0.17–0.37	0.90–1.20	$\leq 0.30$	$\leq 0.15$	Bal

The composition of the Fe-based alloy powder in the experiment is shown in Table 2. The Fe-based powder and different content of Mo powder were mixed for 2–4 h using a ball mill to make the various elements uniformly. The mixed powder was put into a drying oven for 6 h to obtain the experimental powder. The powder is a spherical powder with good fluidity, which size is 20–200  $\mu\text{m}$ , Hall flow is less than 45 s/50 g. The laser cladding coating was prepared by LAM-400S synchronous powder feeding laser. The laser cladding process parameters are shown in Table 3. To ensure operational safety and prevent the oxidation of the material in the high temperature cladding process, the whole preparation processes were completed in a vacuum environment. Finally, the cladding layer with the size of  $50\text{ mm}\times 5\text{ mm}\times 1\text{ mm}$  is obtained.

### 2.2 Analysis methods

The microstructure and phase composition of the coating were characterized by scanning electron microscopy (SEM) and X-ray diffraction (XRD). The hardness of the coating and 65Mn was tested by 402MVD Vickers microhardness tester, which the load was set to 120 g and the loading time was set to 15 s. Impact tests were carried out on 65Mn and Fe–Mo alloy coatings using the JBN-300C

**Table 2** Chemical composition of Fe-base alloy powder (wt.%)

Coating	Mo	Si	Cr	C	Ni	Co	Fe
Fe–5Mo	5	2	10	1.5	14	4	Bal
Fe–10Mo	10	2	10	1.5	14	4	Bal
Fe–15Mo	15	2	10	1.5	14	4	Bal

**Table 3** Laser cladding process parameters

Process parameter	Value
Laser power (W)	1000
Laser scanning speed (mm/min)	600
Spot diameter (mm)	1
Absorption rate (%)	25
Overlapping (%)	45

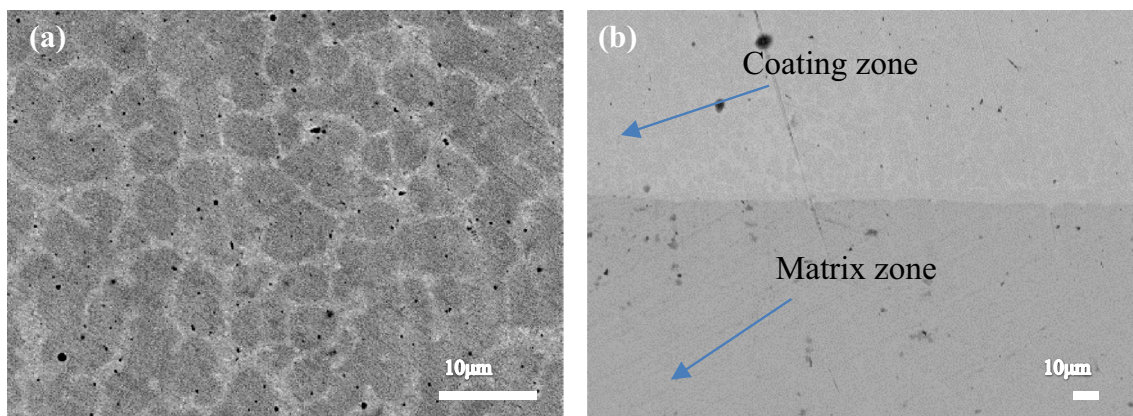
pendulum impact tester to simulate the impact toughness of ploughshares when subjected to hard impacts during ploughing. The friction coefficient of the coating was measured by RTECMFT-3000 friction tester with a force of 60 N, a reciprocating stroke of 10 mm, and a wear time of 3600 s. GCr15 steel balls with a diameter of 6.35 mm and a hardness of 62HRC are used for the grinding parts. The friction and wear properties of the coating in soil environment were tested by MLD-10 dynamic load abrasive wear tester. The plow moldboard was mainly subjected to erosion abrasive wear. In the erosion abrasive wear test, the specimen was clamped on a disc-shaped fixture, the transmission shaft drove the specimen to rotate in the sand hopper, the tester speed was 200 r/min, the distance between the outermost edge of the specimen and the center of the rotating shaft was 80 mm, and the speed of the outermost edge was 6 km/h. The ploughshare was mainly subjected to impact abrasive wear. In the impact abrasive wear test, the wear parts were made of quenched 45 steel, the impact frequency was set to 200/min, the speed was set to 200 r/min, the abrasive

material was quartz sand with a particle size of 0.5–5 mm, the abrasive flow rate was 30 kg/h, and the impact energy was 0.5 J/cm<sup>2</sup>. During the test, the hammerhead moved up and down repeatedly to impact the specimen, while abrasive material flowed into the contact surface between the upper and the lower specimens to complete the impact. The corrosion resistance of 65Mn and Fe–Mo alloy coatings were investigated using a CHI604E electrochemical workstation with a three-electrode system. The saturated calomel electrode was used as the reference electrode, the platinum plate was used as the auxiliary electrode, and the specimen was used as the working electrode, effective working area of test piece is about 1 cm<sup>2</sup>. The simulated soil electrolyte solution was composed of 0.483 g/L NaHCO<sub>3</sub>, 0.122 g/L KCl, 0.137 g/L CaCl<sub>2</sub>, 0.131 g/L MgSO<sub>4</sub>, and 0.5 g/L urea.

### 3 Results and discussion

#### 3.1 Microstructure analysis

The surface and cross-section SEM of the coating are presented in Fig. 2, there are no obvious cracks, faults and other defects, only a few pores. In addition, the uniform white mesh structure was found from the morphology. Figure 3 shows that the content of Mo and Cr in the white mesh structure is much higher than that other regions, which may be due to the fact that the Mo and Cr have undergone segregation at the grain boundary, and the grain boundary structure is looser than in the grain, with

**Fig. 2** Surface and cross-section SEM of the coating. **a** Surface and **b** cross-section

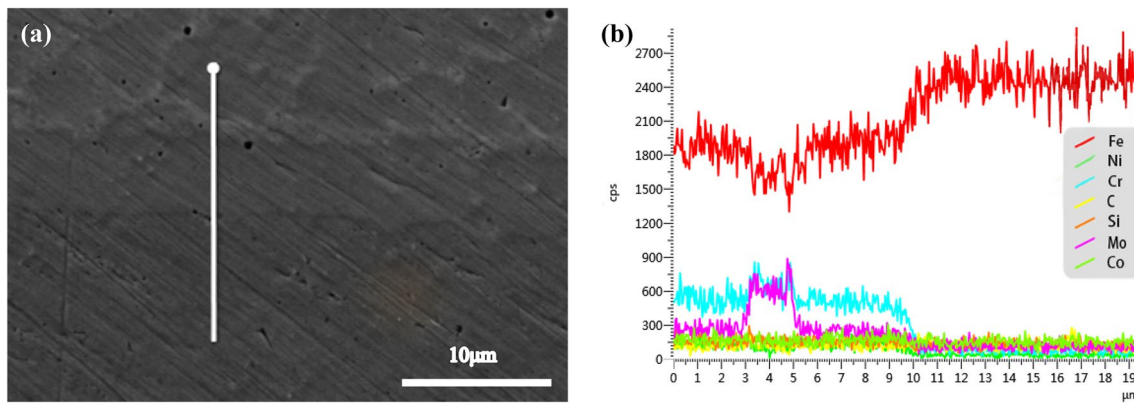


**Fig. 3** EDS line on cross-section of the coating

certain surface effects. The energy of Cr and Mo atoms in the grain is higher than that in the grain boundary, and there is a tendency of spontaneous segregation to the grain boundary, which reduces the energy of the system and satisfies the heterogeneous nucleation [18]. At the grain boundary, Mo can attract Cr at other positions to migrate to the grain boundary and form eutectics with C and other

elements, which can enhance the bonding strength of the grain boundary [19].

As can be seen from the EDS map of the bonding area between the coating and the matrix in Fig. 4, there is an obvious delamination of Mo, Ni, Cr, and Fe, with Mo and Cr occur grain boundary segregation and the other elements evenly distributed and without agglomeration, indicating

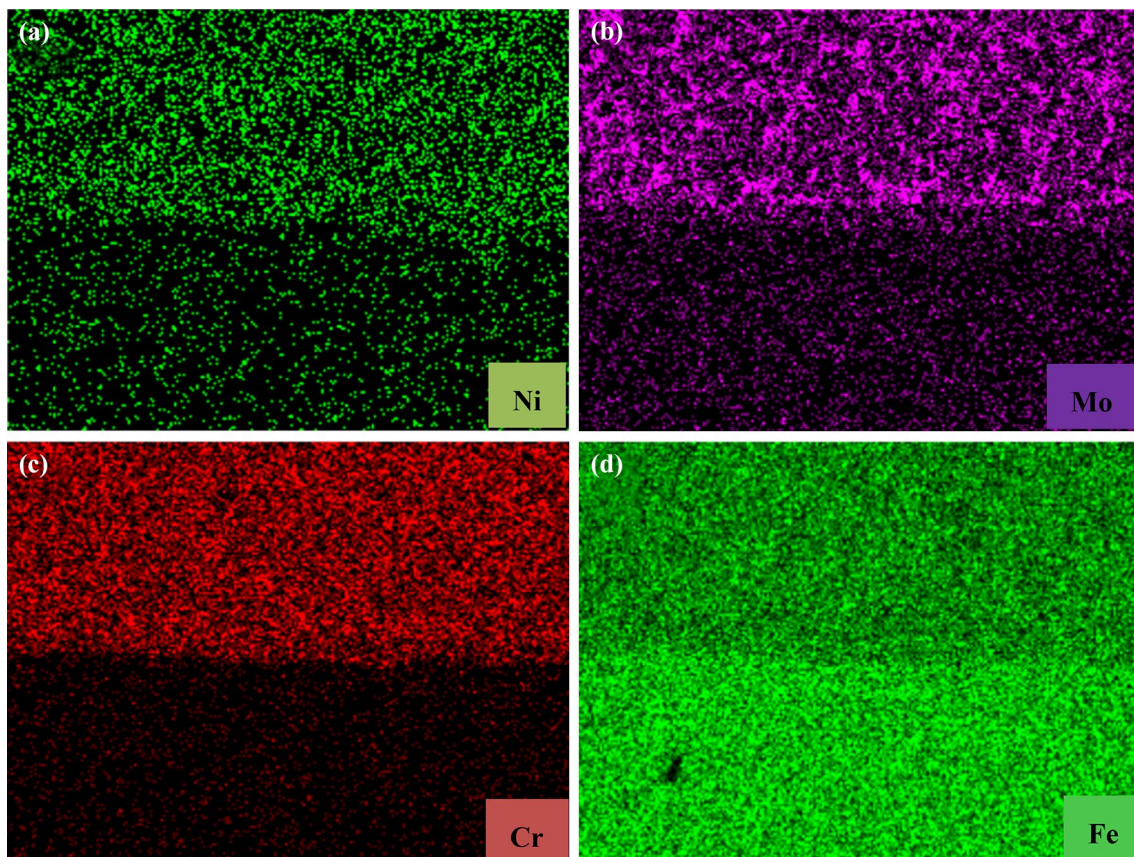


**Fig. 4** EDS map on the bonding area between the coating and the matrix. **a** Ni, **b** Mo, **c** Cr and **d** Fe

that the uniformly distributed alloy structure and reinforcement phase are formed in the coating.

Figure 5a–d shows the surface microstructure of Fe–Mo alloy coatings. When there is no Mo in the alloy powder, the microstructure is dominated by coarse columnar crystals, accompanied by a small number of equiaxed crystals. When the Mo content is 5%, the microstructure is dominated by equiaxed crystals. When the Mo content is 10%, dendritic crystals begin to appear, which is in a state of co-existence of equiaxed and dendritic crystals. When the Mo

content is 15%, it can be found that the microstructure is dominated by a fine and developed dendritic network, with the dendrites growing in the form of equiaxed dendrites. Compared with the microstructure of the coating without Mo, with the increase of Mo, the formation of dendrites is promoted, and the dendrites became finer. The increase in the Mo content has the effect of refining the grain size and promoting nucleation.

Observing the microstructure of the coating after corrosion, it can be seen that three typical areas are created after

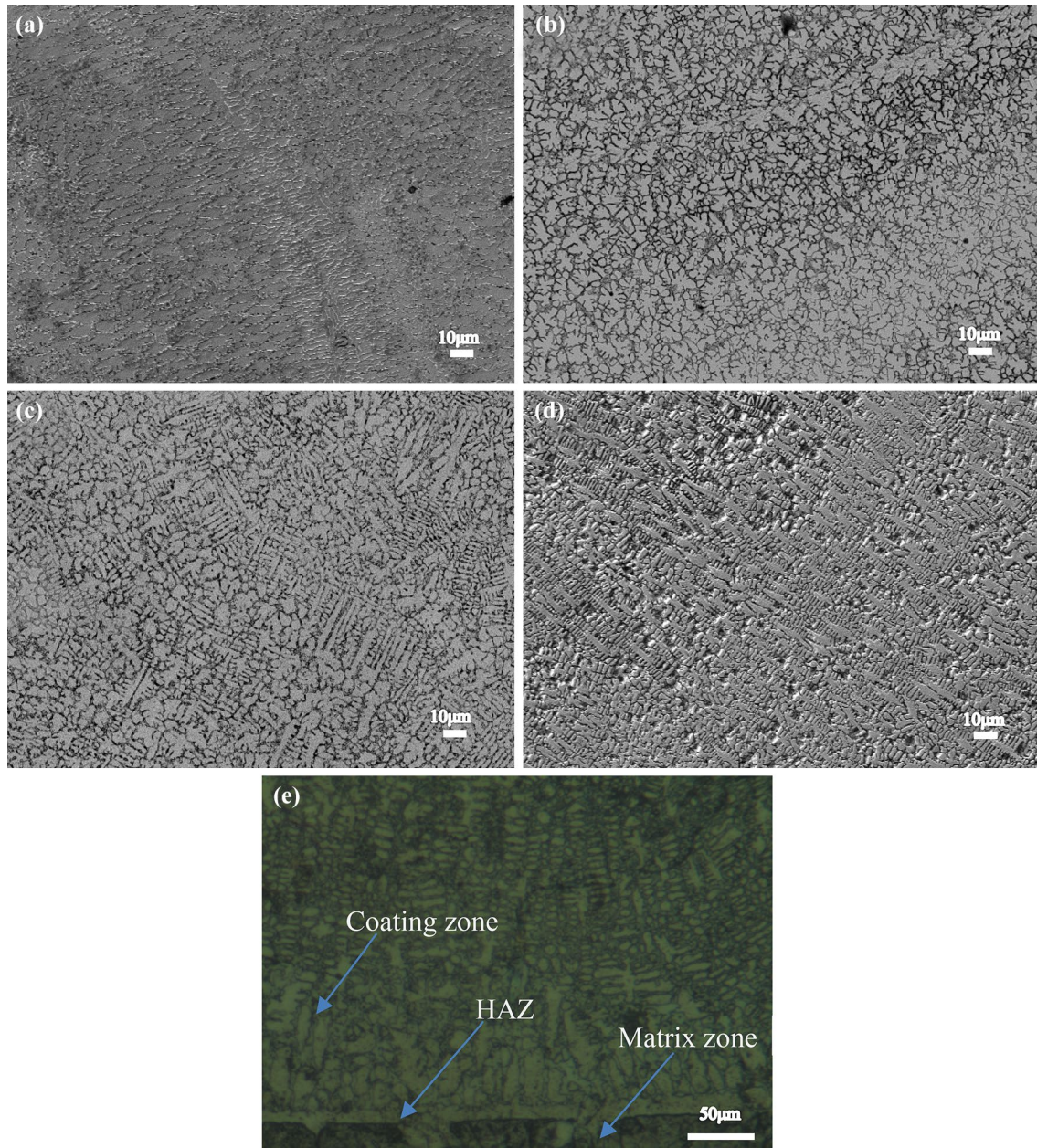


**Fig. 5** Microstructure of Fe–Mo coatings. **a** Fe–0Mo coating surface, **b** Fe–5Mo coating surface, **c** Fe–10Mo coating surface, **d** Fe–15Mo coating surface and **e** Fe–15Mo coating cross-section (after corrosion)

laser cladding, namely the coating area, the heat affected zone (HAZ), and the matrix area. As shown in Fig. 5e, a bright planar crystal band appears in the HAZ at the junction of substrate heat affected zone and coating. Due to the large ratio of temperature gradient to solidification rate in the bonding zone, the heat is transmitted from top to bottom during laser processing, while the microstructure is grown from bottom to top, which makes the microstructure of the HAZ flat and slow to grow, forming a planar crystal. This is the product of the transient liquid diffusion of 65Mn and Fe–Mo alloy coatings, indicating that the coating and the matrix form a good metallurgical bonding, Lin et al. [20] analyzed a series of tests such as residual stress test, wear test and corrosion test, and showed that SMA/PZT composite coating was prepared on 304 stainless steel by laser cladding technology. The coating formed a fine metallurgical bond with the substrate, and the microstructure consisted of planar crystal, cell crystal, dendrites and equiaxed crystals. Liu et al. [21] showed that laser surface cladding is a process technology for depositing alloy layer on the surface of metal substrate. Laser cladding produces good metallurgical bonding between coating and workpiece, so it is widely used in the repair and manufacturing of three-dimensional parts. The matrix has been corroded into dark black because of poor corrosion resistance, which also indicates that the coating has better corrosion resistance.

Figure 6 shows the XRD patterns of Fe–Mo alloy coatings. The alloy coating mainly contains Cr–Ni–Fe–C and Fe–Cr solid solutions,  $\text{Cr}_7\text{C}_3$  and  $\text{Mo}_2\text{C}$  carbides, and  $\sigma$ -phase. The  $\sigma$ -phase consists of  $\text{Co}_7\text{Mo}_6$ ,  $\text{CoMo}_2\text{Ni}$ ,  $\text{Cr}_9\text{Mo}_{21}\text{Ni}_2$  and other metal compounds Mao et al. and Liu et al. [22, 23] showed in their research conclusions that the main components of the coating are various alloy solid solutions and uncertain components  $\sigma$  Phase composition,

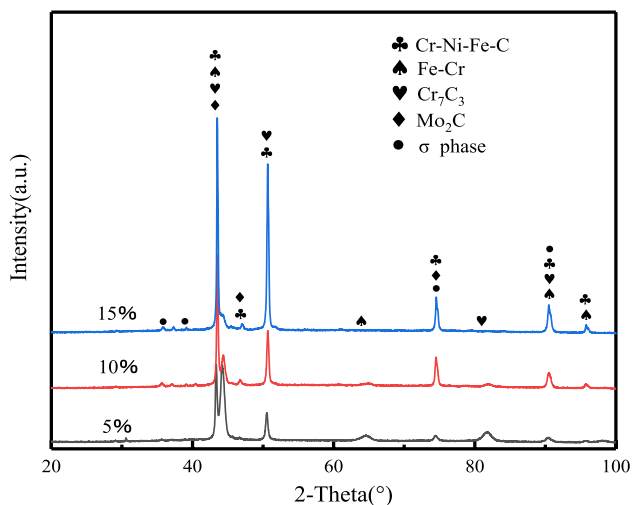


Fig. 6 XRD pattern of Fe–Mo coatings

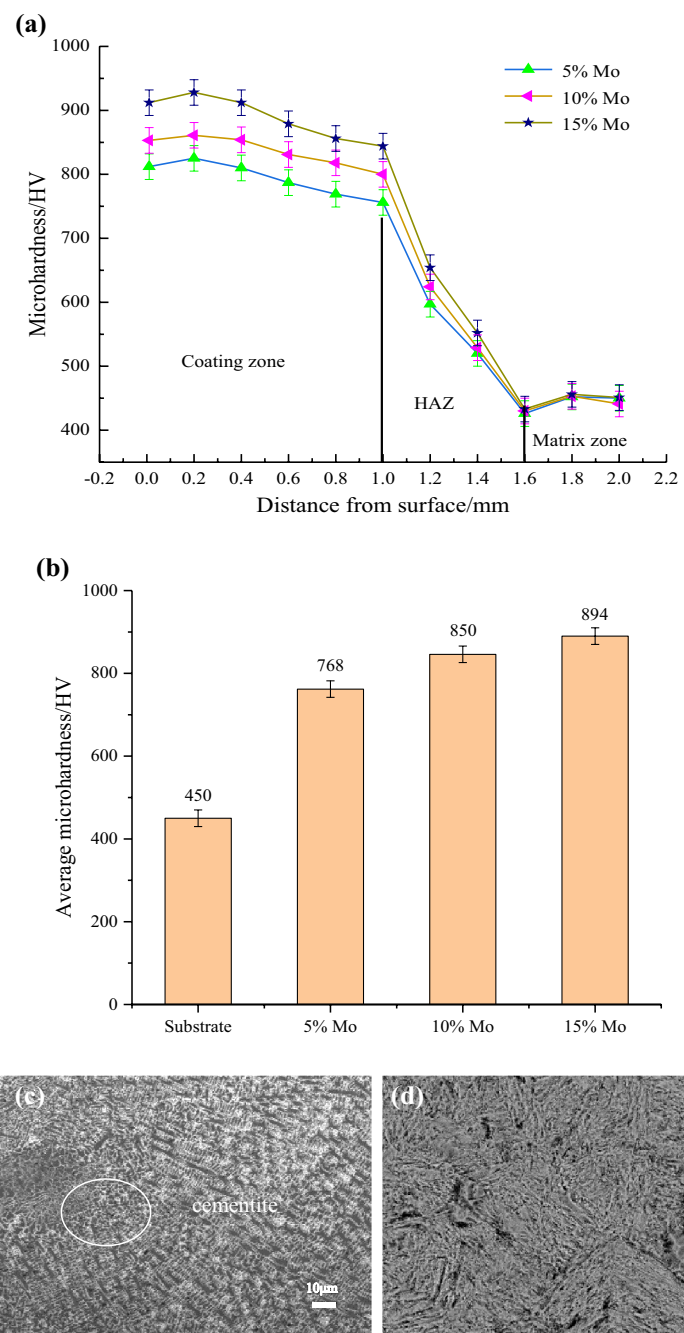
and Mao shows that Y doping will lead to lattice distortion of solid solution, resulting in the transformation of double BCC phase into single BCC phase. These solid solutions and compounds will produce lattice distortion, which causes the mutual reinforcement between metal elements. The  $\sigma$  phase belongs to brittle phases, which are amorphous alloy replacement solid solutions such as carbide or intermetallic compounds. They have a great effect on improving the hardness of the coating, but too much  $\sigma$  phase will reduce the plasticity and toughness and increase the cracking sensitivity. However, the research shows that Ni can expand the austenite zone, so adding a certain amount of Ni can reduce the content of austenite in the alloy coating  $\sigma$  the tendency of phase formation. The enthalpy of Mo is relatively small, and it is easy to combine with other elements to form compounds, and a small amount of Mo can also be solubilized in  $\alpha$ -Fe, resulting in a certain solid solution strengthening of the matrix. As the coating cools, supersaturated Cr and Mo precipitate out of the grain boundary, generating compounds such as  $\text{Cr}_7\text{C}_3$  and  $\text{Mo}_2\text{C}$ . These carbides have excellent wear resistance and corrosion resistance and will not grow up, so as to improve the hardness.

### 3.2 Hardness analysis

Figure 7 shows the hardness variation pattern of the alloy coating. From Fig. 7a, it is found that the microhardness decreases gradually from coating surface to HAZ and then to matrix. This is due to the fact that the reinforcing phase is subjected to a flow field during the laser cladding process, which makes it easy to float on the top of the molten pool, reducing the proportion of reinforcing phase at the bottom of the coating and thus reducing the hardness. From the coating to the HAZ, the hardness decreases relatively slowly and there are no obvious step changes, which indicates that the microhardness distribution in the coating zone is relatively uniform. It can also be seen that the maximum hardness of the coating does not occur on the outermost surface. This is because during the laser cladding process, the rapid cooling of molten pool leads to the accumulation of impurities and voids to the coating surface, which reduces the strength. In the heat affected zone, hardness drops suddenly faster. On the one hand, this is due to the gradual reduction of the reinforcing phase. On the other hand, the matrix with low hardness and the cladding material are remelted and crystallized, which reduces the strength. Since the matrix has been heat treated before laser cladding, the hardness is slightly higher than that of the HAZ where the matrix zone meets the HAZ. The above analysis shows that the hardness of Fe–Mo alloy coating is much higher than that of 65Mn matrix, which can meet the requirements of ploughshares.

As seen in Fig. 7b, the average microhardness of the matrix surface is 450 HV and the highest average

**Fig. 7** The hardness variation pattern of the coatings. **a** Microhardness variation pattern, **b** average microhardness of the matrix and the coating, **c** microstructure of the coating and **d** microstructure of the matrix



microhardness of the Fe–Mo alloy coating is 894 HV, which is nearly a twofold increase in hardness compared to the matrix. The SEM microstructure of the coating surface and the matrix are shown in Fig. 7c, d. It can be seen that the microstructure of the coating is fine equiaxed crystal. And the microstructure of the matrix is tempered sorbite, which contains large particles of cementite. The grain size was measured by Imagetool (a free image processing and analysis program). The average grain size of the matrix microstructure is 10 μm, and that of the coating microstructure is 5 μm. Then, according to the Hall–Petch relationship [24],

the strength of the material will double when the size of the microstructure grain is refined by one grade, which further demonstrates that the hardness of the coating is much higher than that of the matrix.

### 3.3 Impact toughness analysis

The composition of soil is complex, and the ploughshare will face complex working conditions. The impact toughness of 65Mn and Fe–Mo coatings were tested. According to the actual use of the ploughshare, it can be carried out at room

temperature without low-temperature impact. The results are shown in Fig. 8. After the impact test, the fracture morphologies of different specimens were observed. By studying the fracture morphologies and fracture mechanism of the matrix and the coating, the fracture can be effectively

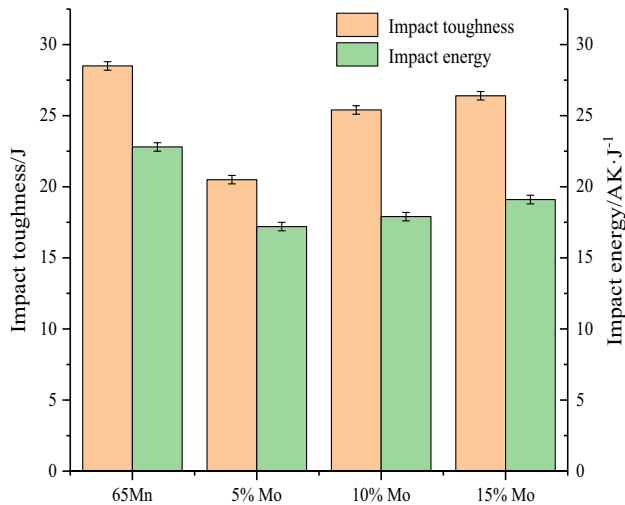


**Fig. 8** Impact resistance of the matrix and the Fe–Mo coatings

prevented and the impact toughness can be improved. Figure 9 shows the fracture morphologies of the bonding area between the matrix and the coating. It can be seen that the fracture morphologies of the matrix and the coating are quite different, but the bonding is firmly and closely. The fracture of the coating is flat and bright, and the surface plastic deformation is small. There is no obvious fiber area, shear lip area, and dimple zone, which belongs to the brittle fracture characteristics. As can be seen from Fig. 10a, the 65Mn macroscopic fracture is relatively flat, the microscopic fracture has a river-like pattern and a small amount of tough dimples, and the tough dimples are surrounded by white rip edge, which are typical of quasi-cleavage fracture. Quasi-cleavage fracture is a mixed fracture between the cleavage fracture and the dimple fracture, which often occurs in the impact fracture of steel at high temperature quenching and low-temperature tempering. The reason for this phenomenon is that the matrix was heat treated before laser cladding, which is equivalent to tempering the matrix during laser cladding [25]. As can be seen in Fig. 10b–d, at low magnification, the impact fractures of the coating exhibit a stony and icing-like appearance, which have cleavage steps. At high magnification, continuous white meshes are precipitated on the coating fracture along the grain boundary.

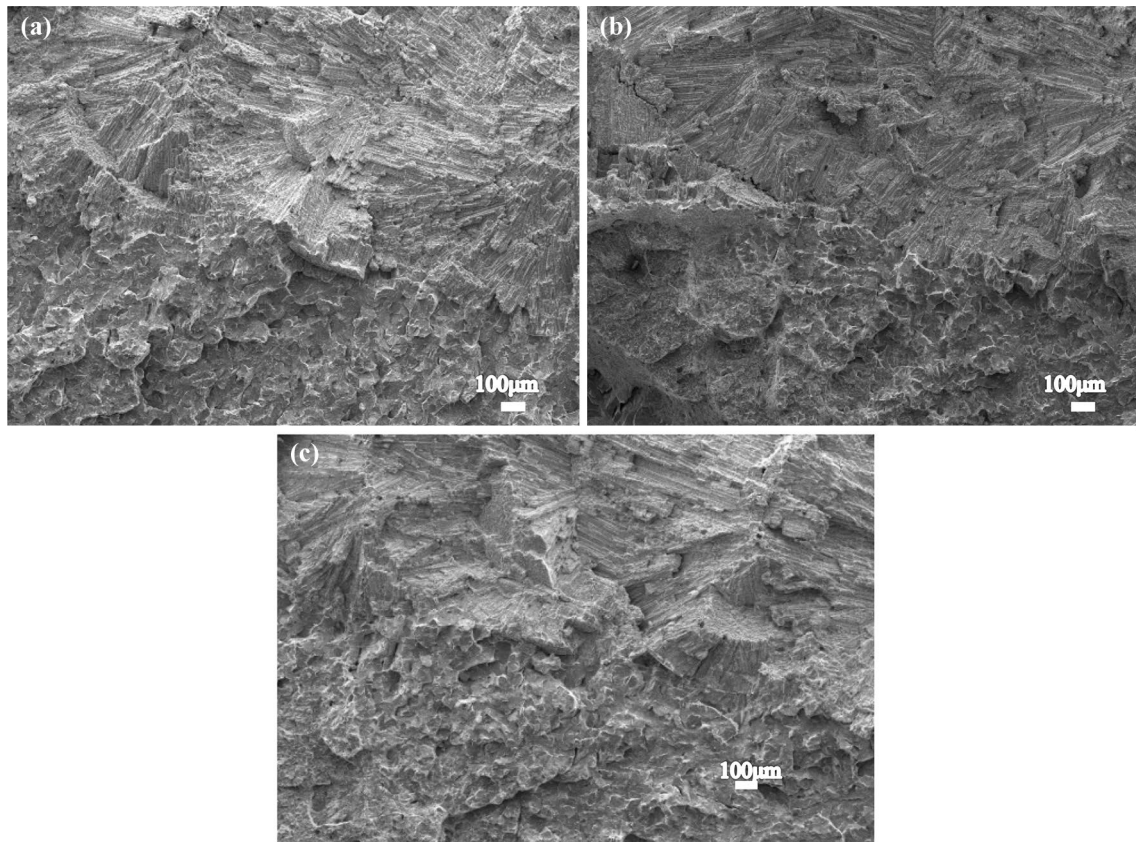


**Fig. 9** Fracture morphologies of the bonded are between the matrix and the coatings. **a** Fe–5Mo, **b** Fe–10Mo and **c** Fe–15Mo



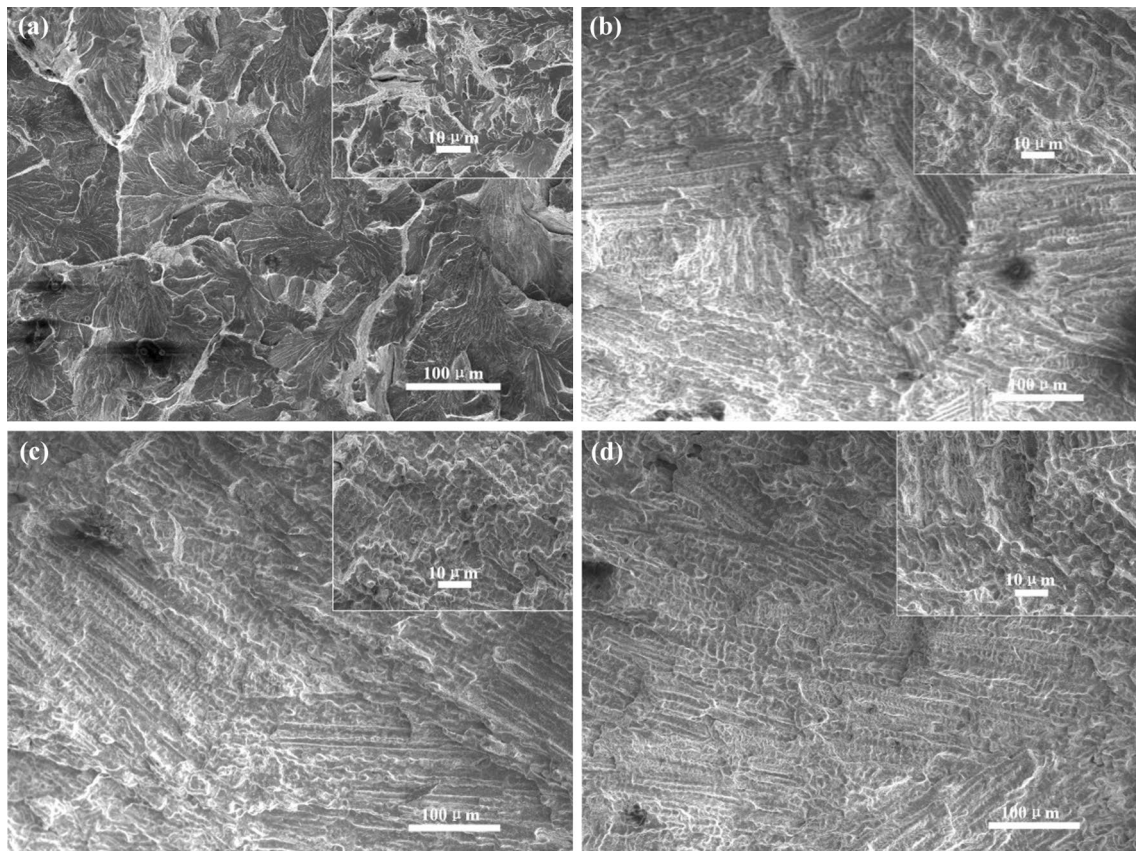


**Fig. 10** Fracture morphologies of the matrix and the coatings under different magnifications. **a** 65Mn matrix, **b** Fe–5Mo, **c** Fe–10Mo and **d** Fe–15Mo

Combined with the above analysis, white meshes are brittle phases containing  $\text{Cr}_7\text{C}_3$ ,  $\text{Mo}_2\text{C}$ , and  $\sigma$  phases. Cracks are easily formed under the action of external force, resulting in brittle fracture along grain boundary on the fracture [26, 27]. It can also be seen that as the Mo content increases, the tough dimples of the coating increases significantly, indicating that Mo can improve the toughness, which is consistent with the impact results.

From the impact results, the impact toughness of 65Mn matrix is 28.5 J, and the impact toughness of Fe–Mo alloy coatings are 26.4 J, 25.4 J, and 20.5 J, respectively. Compared with the matrix, the impact toughness of the coating decreases slightly while the hardness is greatly improved. It can be seen from the impact morphology that Mo can play a positive role in improving the toughness of the coating.

### 3.4 Wear resistance analysis

The friction coefficient of the matrix and the coating are shown in Fig. 11. The average friction coefficient of the coating is 0.23, and that of the 65Mn matrix is 0.36. The friction coefficient of the cladding coating is greatly reduced compared with the matrix. It can be seen from Fig. 12 that the

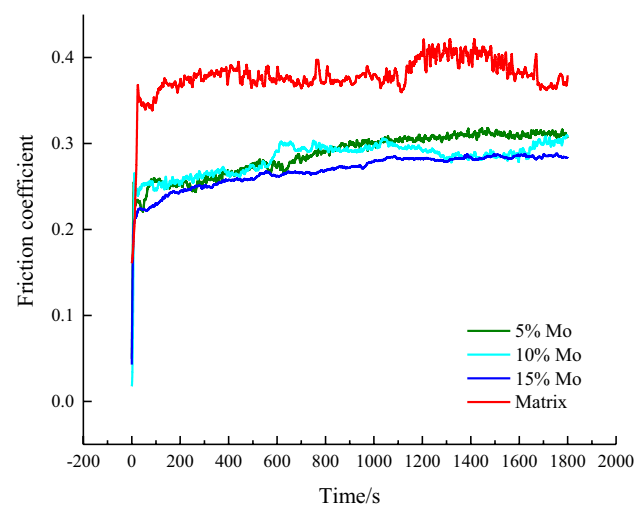


**Fig. 11** Friction coefficient of the matrix and the coatings

impact wear loss of the coating is slow at the initial stage, and wear speeding up after a period of time. In combination with the previous hardness variation of the coating, this is because the coating surface has high hardness, the wear

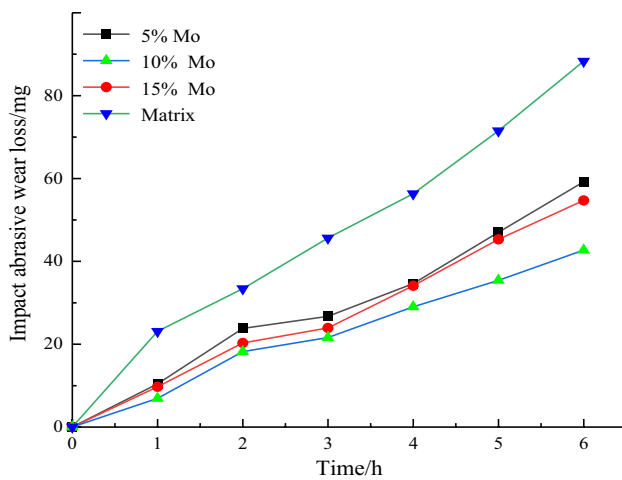


**Fig. 12** Impact abrasive wear loss of the matrix and the coatings

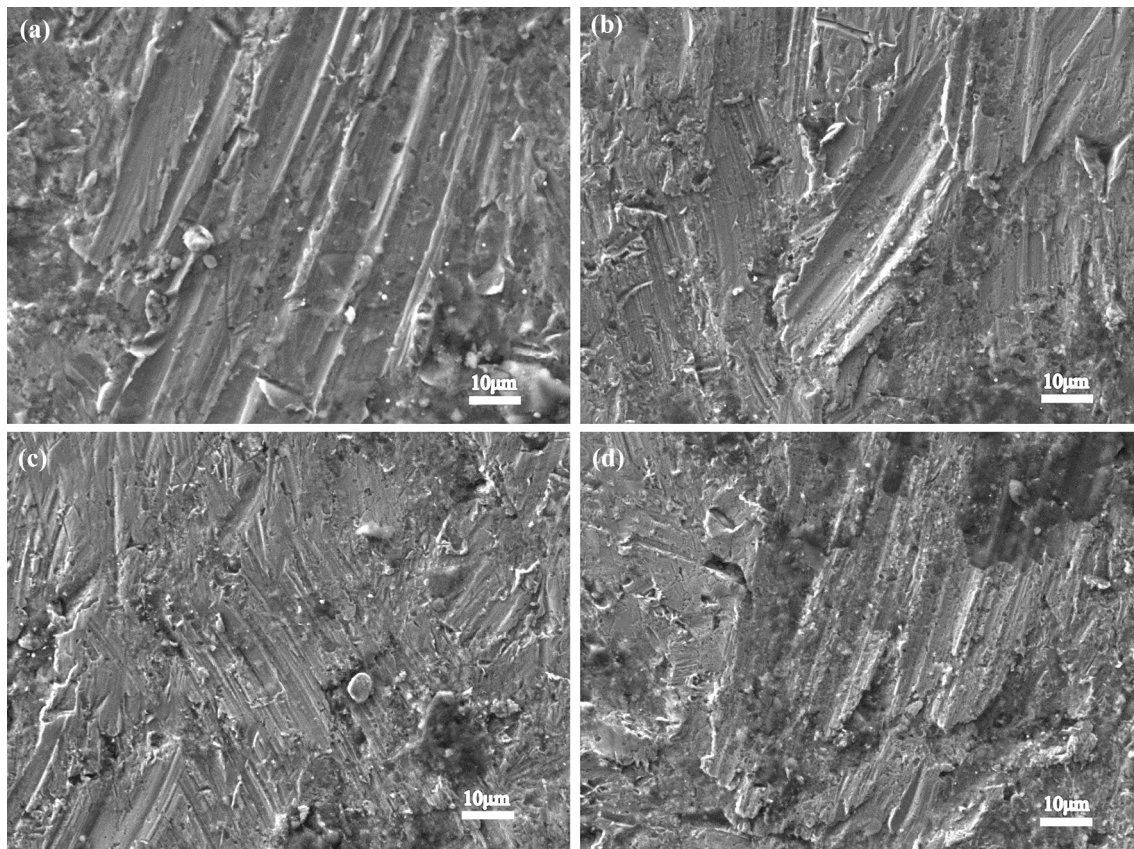
loss is relatively small at the initial stage. As the wear time increases, the external coating is gradually worn away, the hardness of the coating surface decreases, which leads to wear speeding up. Under the same wear conditions, the wear rate of 65Mn is 14.7 mg/h. With the increase of Mo, the wear rates of the coatings are 9.87 mg/h, 7.1 mg/h, and 9.1 mg/h, respectively. The mass loss of 65Mn steel without cladding layer is the most serious, and its impact wear resistance is the worst. The wear loss of the coating is significantly less than that of the matrix, and the impact wear resistance is greatly improved. It can also be seen from the above results that as the Mo increases, the wear rate of the coating first increases and then decreases, there is no monotonic increase like surface hardness. When the Mo content is 15%, obvious cracks appear on the coating surface, which will reduce the coating strength to some extent. When the large particles impact the edge of the cracks, the cracks expand, and the material generates fatigue spalling, resulting in pits on the surface. At this time, the coating is more likely to fall off and the wear loss will increase.

Figure 13 shows the impact abrasive wear morphologies of the matrix and the coatings. It can be seen that under the action of impact abrasive wear, the failure of the surface is caused by both drilling wear and cutting furrow wear, whether the matrix or the coatings. The impact abrasive wear simulated by the dynamic load abrasive wear tester is consistent with the actual working condition of the ploughshare, which belongs to the form of three-body abrasive wear. There are free abrasive grains between the grinding specimen and the lower specimen, and the abrasive grains will roll or slide on grinding specimen. The normal load is different from the normal static load and alternating load, and the abrasive grains have the dual effect of drilling and crushing on friction pair, making the wear more serious [28]. In the impact abrasive wear, the surface of the wear

specimen is subjected to a predominantly vertical impact of abrasive grains. Plastic deformation occurs on the material surface under contact compressive stress, resulting in pits. At the same time, under the action of the impact force, the abrasive cuts into the surface layer of the specimen and slides against it. When the impact force exceeds the strength limit of the material, furrow scratches will occur on the material surface [29–31]. In addition, due to the repeated impact extrusion by abrasive, stress concentration occurs in the plastic deformation area around the furrow. At the same time, when the abrasive impacts the specimen, part of the kinetic energy will be converted into thermal energy to soften the material surface. This will make the material surface fatigue wear and fatigue shedding. It can be seen from Fig. 14, that there are a large number of Si, Ca, O, and other elements on the wear surface, especially in the drilling pits, and during the abrasive impact of the quartz sand, creating a mosaic at the bottom of the pits or cracks, which cannot be completely removed during cleaning, thus remaining on the surface of the specimen. This inlaying behavior of the abrasive also increases the plastic deformation of the material and accelerates the wear.

The impact wear mechanism of the material shows that the wear resistance of the coating can be improved by increasing the hardness of the coating material and ensuring a certain material toughness to resist fatigue deformation and falling off. The reason why the impact abrasive wear resistance of Fe–Mo alloy coatings is better than that of 65Mn matrix is that Cr–Ni–Fe–C and Fe–Cr solid solution, Cr<sub>7</sub>C<sub>3</sub> and Mo<sub>2</sub>C carbides, and  $\sigma$ -phase are formed, which makes the hardness much higher than that of the matrix. In addition, some Mo and Cr oxides generated in the wear process also have the effect of reducing the friction coefficient. The coating also contains appropriate amounts of Ni, Co, and other elements, increasing the austenite phase to balance the brittle material such as  $\sigma$ , ensuring the toughness, and reducing the fatigue cracks and fatigue wear during the impact process. The Fe–Mo alloy coating is therefore able to meet the actual working requirements of ploughshares.

Figure 15 shows erosion abrasive wear loss of the matrix and the coatings. It can be seen that the change law of wear amount of cladding coating is different from that of impact wear. The wear rate is initially slow, and after a period of time, the wear speeding up, which was similar to the impact test. However, in the latter half of the wear, the wear rate decreases significantly, which is due to the different methods of erosion and impact wear experiments. The erosion abrasive wear is caused by the uniform rotation of the specimen with the rotating shaft in the abrasive grains. The impact of the abrasive grains is relatively small, as time increases the angles of the larger grains become rounded and smaller, and the impact kinetic energy decreases. So the wear rate increases first and then decreases. Under the same wear



**Fig. 13** Impact abrasive wear morphologies of the matrix and the coatings. **a** 65Mn matrix, **b** Fe–5Mo, **c** Fe–10Mo and **d** Fe–15Mo

conditions, the 65Mn substrate has an erosion wear rate of 9.05 mg/h. The wear rates of the coatings are 6.4 mg/h, 5.8 mg/h, and 4.6 mg/h with increasing Mo, where the mass loss and wear rate of 65Mn are much larger than the coatings. This indicates that the erosion resistance of the coating is much better than that of 65Mn, and the erosion wear resistance increases with the increase of Mo.

The erosion abrasive wear morphologies of the matrix and the coatings are shown in Fig. 16. It can be seen that the erosion abrasive wear morphologies of the coating and the substrate are mainly furrow scratches, and its mass loss is relatively small compared to impact abrasive wear. Among them, 65Mn has the most severe wear and the greatest depth of furrows. When the content of Mo is 15%, the furrows and scratches are the least and the abrasive wear resistance is the best. This indicates that Mo has a significant effect on the resistance of the coatings to erosion abrasive wear. The main difference between impact abrasive wear and erosion abrasive wear is that the action angles between abrasive and specimen are different, which is  $90^\circ$  for impact abrasive wear and  $0^\circ$ – $90^\circ$  for erosion abrasive wear. In the erosion abrasive wear, the impact force is substantially reduced due to the acute angle of the abrasive grains on the wear surface, which is mainly manifested as the cutting force [32, 33]. According

to the actual working conditions of the ploughshare, the plough tip plays a role in cutting off the soil and pushing it upwards along the ploughshare, then throwing the soil over. The plough tip is mainly subjected to the impact abrasive wear of soli hard particles. There is an acute angle when the middle part of ploughshare contacts with the soil hard particles. The soil particles have a trend of tangential slip, which the impact force is weakened. The middle of ploughshare is mainly subjected to erosion abrasive wear [34]. Through the above analysis of abrasive wear, it can be seen that the wear experiment conforms to the actual working condition of ploughshare and achieves the purpose. At the same time, the wear performance of the Fe–Mo alloy coatings has been greatly improved to meet the requirements of ploughshare.

### 3.5 Corrosion resistance analysis

As can be seen from Fig. 17 and Table 4, the corrosion current of the coating is two orders of magnitude smaller than that of the matrix, indicating that the coating has superior corrosion resistance. As can be seen from Fig. 18, at the initial stage of corrosion, the electrode potential of both the coating and the matrix shows a significant decrease, after a period of time, the potential of the coating tends to be stable,

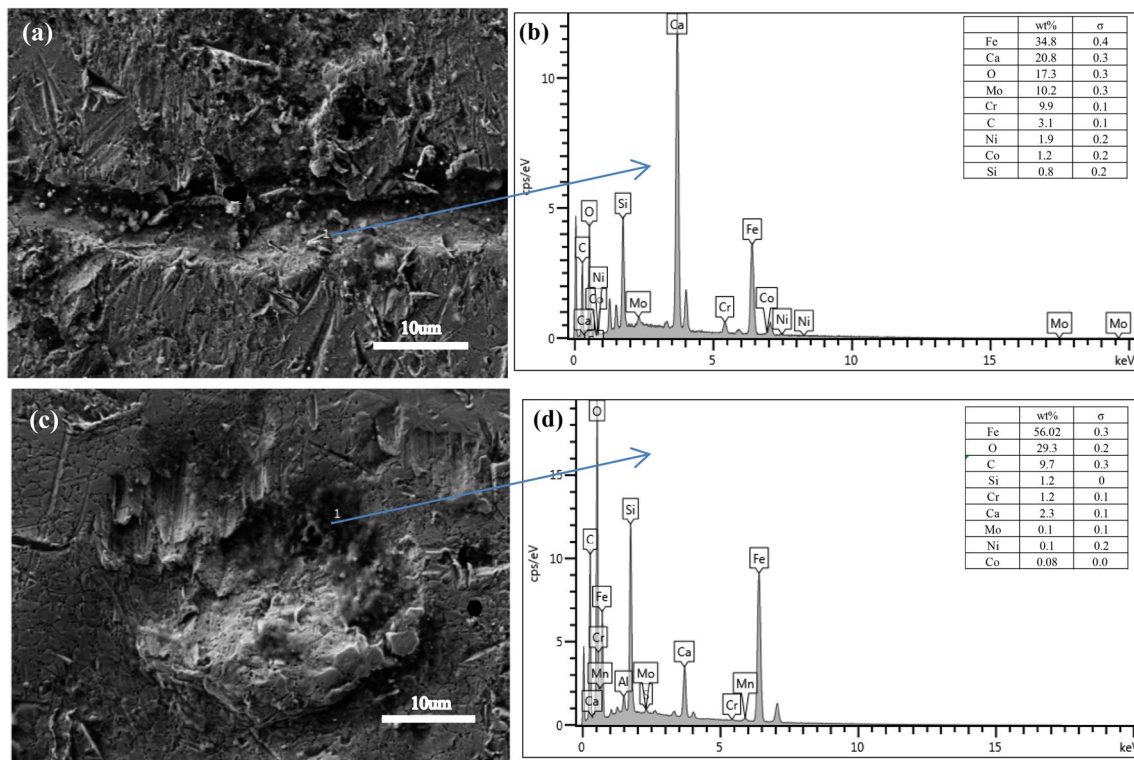


Fig. 14 EDS on impact abrasive wear surface of the matrix and the coatings

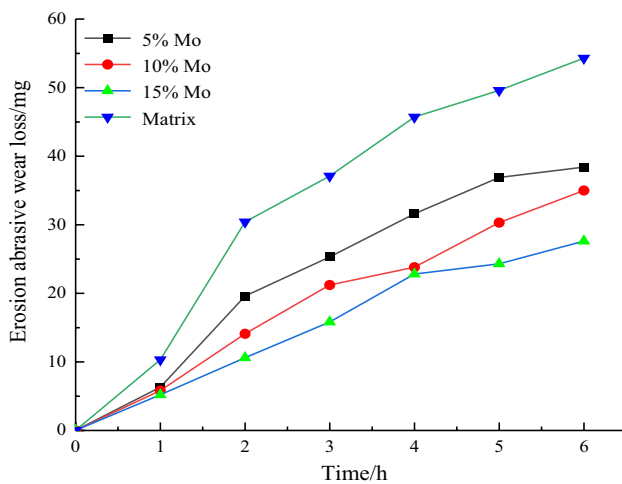
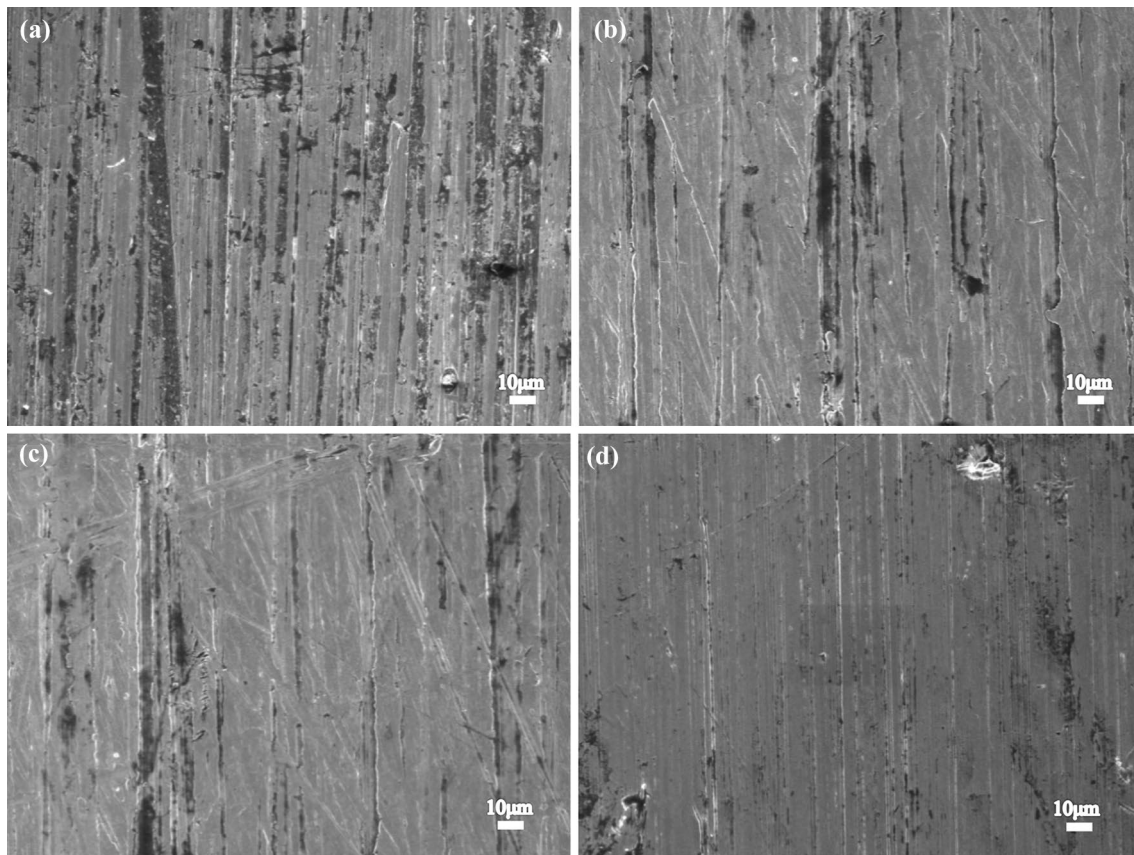


Fig. 15 Erosion abrasive wear loss of the matrix and the coatings

indicating that the coating surface begin to produce passive films with a wide passivation interval  $\Delta E_p$ . As a result, Fe–Mo alloy coatings have better corrosion resistance. The meanings of the symbols in the figure and table are respectively the slope  $B_a$  of anode polarization curve, the slope  $B_c$  of cathode polarization curve, corrosion potential  $E_{corr}$ , corrosion current density  $i_{corr}$  and pitting potential  $E_{pit}$ . Lal et al. [35] explained the existence of salt and organic matter

in the soil by the impact of plow on the soil. Therefore, the protection of plowshares is also very necessary. Zhou et al. [36] used embedded powder method to laser cladding FeSiB, FeSiBCr and FeSiBCrMo coatings on the surface of S355 steel. The effects of adding Cr and Mo on the immersion corrosion and electrochemical properties of the coating in 3.5 wt% NaCl solution for 720 h were analyzed. Through the analysis, it was found that the addition of Cr accelerated the formation of  $Cr_2O_3$  passive film, and the addition of Mo further improved its stability, which is the main factor to improve the corrosion resistance. Xu et al. [37] prepared iron-based powder multilayer coatings mixed with different elements on the surface of 4Cr5MoSiV1 steel by laser cladding method, and then tested and analyzed the mechanical properties and electrochemical corrosion properties. The results show that the introduction and increase of Ni in Fe-based alloy significantly improve the impact toughness of the cladding layer and show high corrosion resistance.

Because the plowshare may work in a corrosive environment, the corrosion resistance of the coating is analyzed. YWX/Q-150 salt spray corrosion test chamber (produced by Nanjing Jinling environmental testing instrument equipment Co., Ltd.) is used for salt spray test. The adjusting temperature is  $35 \pm 2$  °C, pH is controlled at 6.5–7.2, the average deposition rate of 80cm<sup>2</sup> horizontal area is 1.5 mL/h + 0.5 mL/h, the concentration of NaCl solution



**Fig. 16** Erosion abrasive wear morphologies of the matrix and the coatings. **a** 65Mn matrix, **b** Fe–5Mo, **c** Fe–10Mo and **d** Fe–15Mo

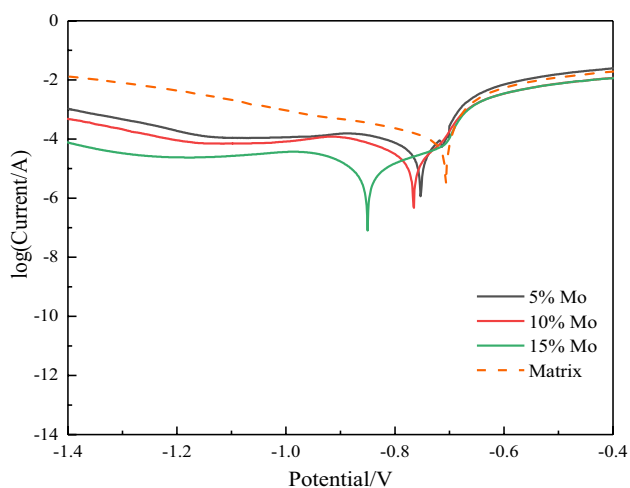


**Fig. 17** Tafel dynamic potential polarization curves of the matrix and the coatings

is  $50 \text{ g/L} \pm 5 \text{ g/L}$ , intermittent spray is used, the 12 h spray wetting + 12 h drying is used as a working cycle, the sample is removed once every two cycles, the surface of the sample is washed with anhydrous alcohol, and the blower dries with cold air. then the sample shall be observed and weighed, and

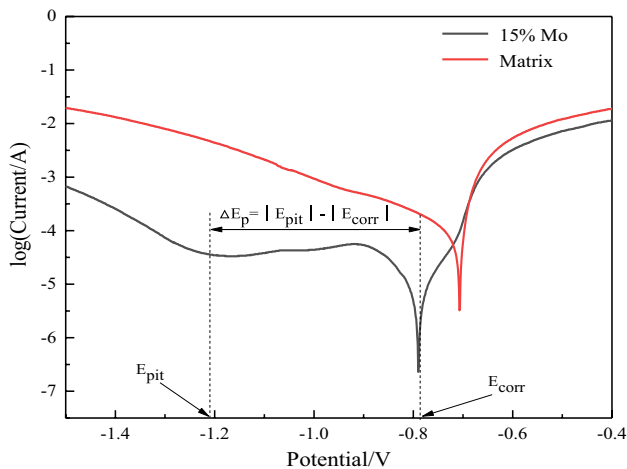
the whole process shall be cycled for three times. Fe–15Mo cladding coating and 65Mn matrix are taken as test objects in this test.

As shown in Fig. 19, a small amount of irregular star shaped corrosion products appears on the surface of A1 sample, which is pitting corrosion in local metal corrosion. With the gradual increase of corrosion time, it can be found that the corrosion area on A2 and A3 surfaces begins to change from pitting to flaky, the corrosion area becomes larger, and the corrosion is more serious. From A4, A5 and A6, it can be seen that the Fe–15Mo cladding coating has good corrosion resistance, no obvious corrosion damage has occurred on the surface, the corroded surface still has metallic luster, and only a small amount of corrosion has occurred where there are physical defects on the surface.

Figure 20 is the histogram of corrosion amount per unit area of 65Mn matrix and Fe–15Mo cladding coating. It can be seen from it that with the increase of corrosion time, the corrosion amount per unit area of 65Mn matrix and cladding coating also gradually increases, but the corrosion rate of 65Mn matrix has an increasing trend with time. It should be considered that when pitting corrosion occurs on the sample surface, pitting corrosion nuclei are formed, that is, corrosion active centers are generated, which makes the corrosion

**Table 4** Electrochemical parameters of the matrix and the coatings

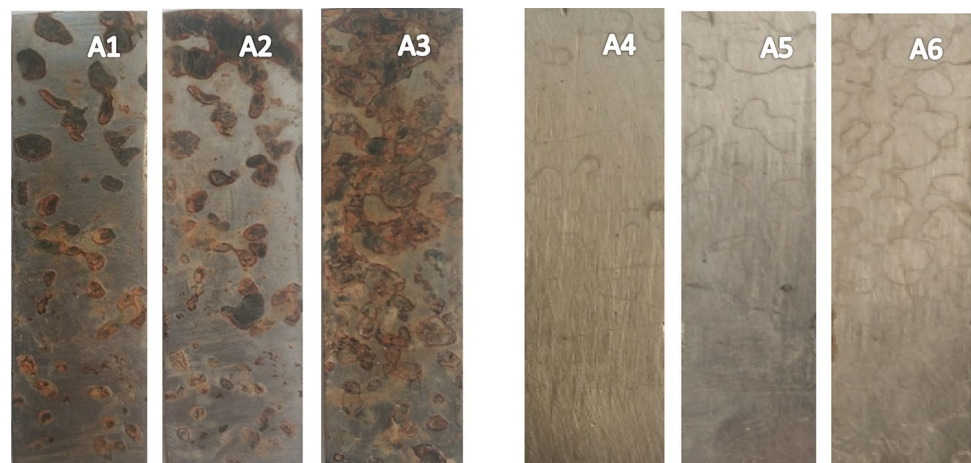
Energy density (J/cm <sup>2</sup> )	$E_{\text{corr}}$ (V vs. Ag/AgCl)	$i_{\text{corr}}$ (A cm <sup>-2</sup> )	$B_a$ (mV dec <sup>-1</sup> )	$B_c$ (mV dec <sup>-1</sup> )
Substrate	$-0.707 \pm 0.06$	$2.56 \times 10^{-4}$	6.920	4.233
5% Mo-Fe	$-0.844 \pm 0.06$	$1.331 \times 10^{-5}$	5.728	3.463
10% Mo-Fe	$-1.036 \pm 0.06$	$1.032 \times 10^{-5}$	2.538	7.462
15% Mo-Fe	$-0.790 \pm 0.06$	$4.726 \times 10^{-6}$	23.909	4.376

**Fig. 18** Tafel dynamic potential polarization curves of the matrix and the coatings

rate of 65Mn steel larger. After 3 days of corrosion under the same corrosion environment, the average corrosion rate of 65Mn steel is  $24 \text{ mg (dm}^2 \text{ d)}^{-1}$ , and the average corrosion rate of cladding coating is  $0.53 \text{ mg (dm}^2 \text{ d)}^{-1}$ . From the corrosion results, the corrosion resistance of Fe–15Mo cladding coating is much better than that of 65Mn matrix.

Figures 21 and 22 respectively show the SEM micro morphology and EDS composition analysis of corrosion characteristic parts of 65Mn matrix and Fe–15Mo cladding coating surface after 72 h corrosion. It can be seen from the EDS

of the sample corrosion product that the corrosion product contains a certain amount of  $\text{Cl}^-$ .  $\text{Cl}^-$  in the salt spray will enter the sample first through the defects in the passivation film, causing the electrochemical reaction inside the sample, destroying the passivation state of the sample, and replacing the oxygen in the oxide layer on the surface of the sample to form the corrosion product. By observing the microscopic corrosion morphology of 65Mn steel, it is found that the salt spray corrosion of 65Mn steel is poor, and obvious corrosion damage has occurred on its surface. Cracks have been corroded at its grain boundaries, mainly intergranular corrosion. In addition, uniform corrosion has also occurred, and the corrosion degree is serious. Compared with the base material, the surface damage of the Fe–15Mo cladding coating is less, and only a small amount of corrosion is found at the surface physical defects, which are laser cladding processing defects. According to the previous analysis, the cladding coating has formed a passive film with good stability and strong adhesion on its surface, which helps to hinder the diffusion of corrosive medium, reduce the pitting sensitivity, and provide protection for the metal materials under the oxide film, thus reducing the corrosion damage of the test sample. However, defects such as oxide film damage and inclusions are easy to exist in the processing defects or edge areas of the cladding coating, resulting in discontinuous passive film and local selective corrosion in the defective parts without passive film protection. Therefore, processing defects should be avoided during coating preparation to reduce such corrosion problems.

**Fig. 19** A1, A2 and A3 A1 and A3 refer to the macro corrosion morphology of 65Mn steel corroded for 1 day, 2 days and 3 days in the salt spray corrosion box: A4, A5 and A6 refer to the macro corrosion morphology of the Fe–15Mo cladding coating corroded for 1 day, 2 days and 3 days in the salt spray corrosion box

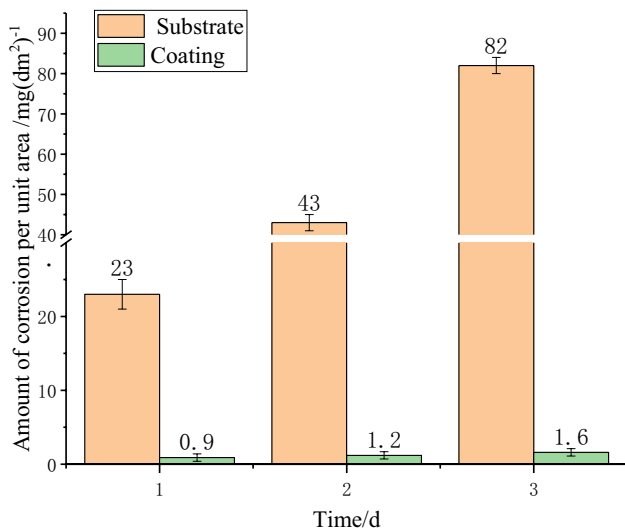


**Fig. 20** Histogram of corrosion amount per unit area of 65Mn matrix and Fe–15Mo cladding coating

Based on the XRD phase analysis of the coating, the coating structure grain has Mo aggregation at the grain boundary, and the Mo segregated to the grain boundary attracts Cr to the grain boundary. Mo that has segregated at grain boundaries also attracts Cr. The Cr that is segregated to the grain boundary can form a dense Cr<sub>2</sub>O<sub>3</sub> passive film, which effectively prevents the further erosion. At the same time, Mo exists in the passive film in the form of MoO<sub>3</sub>, which is conducive to increasing the stability of the passive film, improving the performance of repair, repassivation and local corrosion resistance, thereby reducing the corrosion degree of grain boundaries. It can also be seen from the XRD phase analysis that the Mo will lead to the precipitation of the σ phase. Generally, σ phase will be dissolved after solid solution at high temperature. However, during laser cladding, the σ phase is sometimes difficult to completely dissolve due to the rapid precipitation. If the σ phase cannot be completely dissolved, it will consume Mo and Cr, which will reduce the overall performance of the coating. Therefore, a certain amount of Ni and Co were added to the coating to balance the ratio of the σ phase. Ni and Co both have good corrosion resistance, where Ni can stabilize austenite and expand the

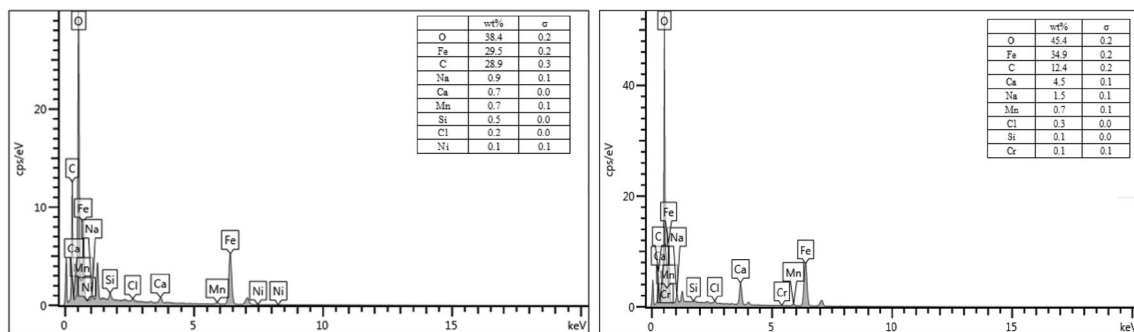
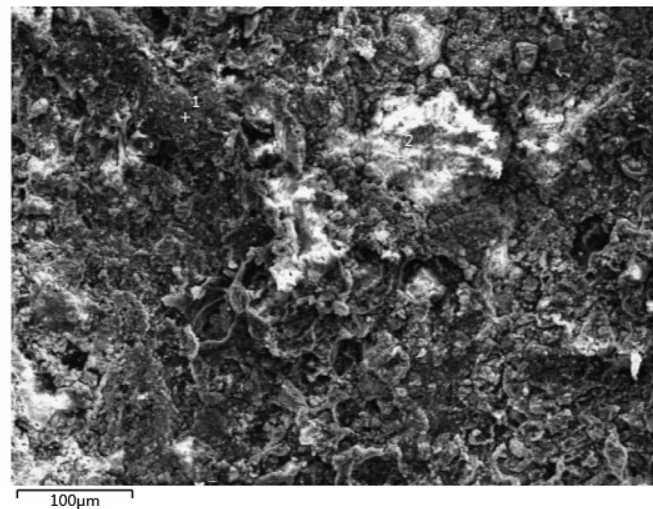


**Fig. 21** SEM and EDS of corrosion products of 65Mn Steel

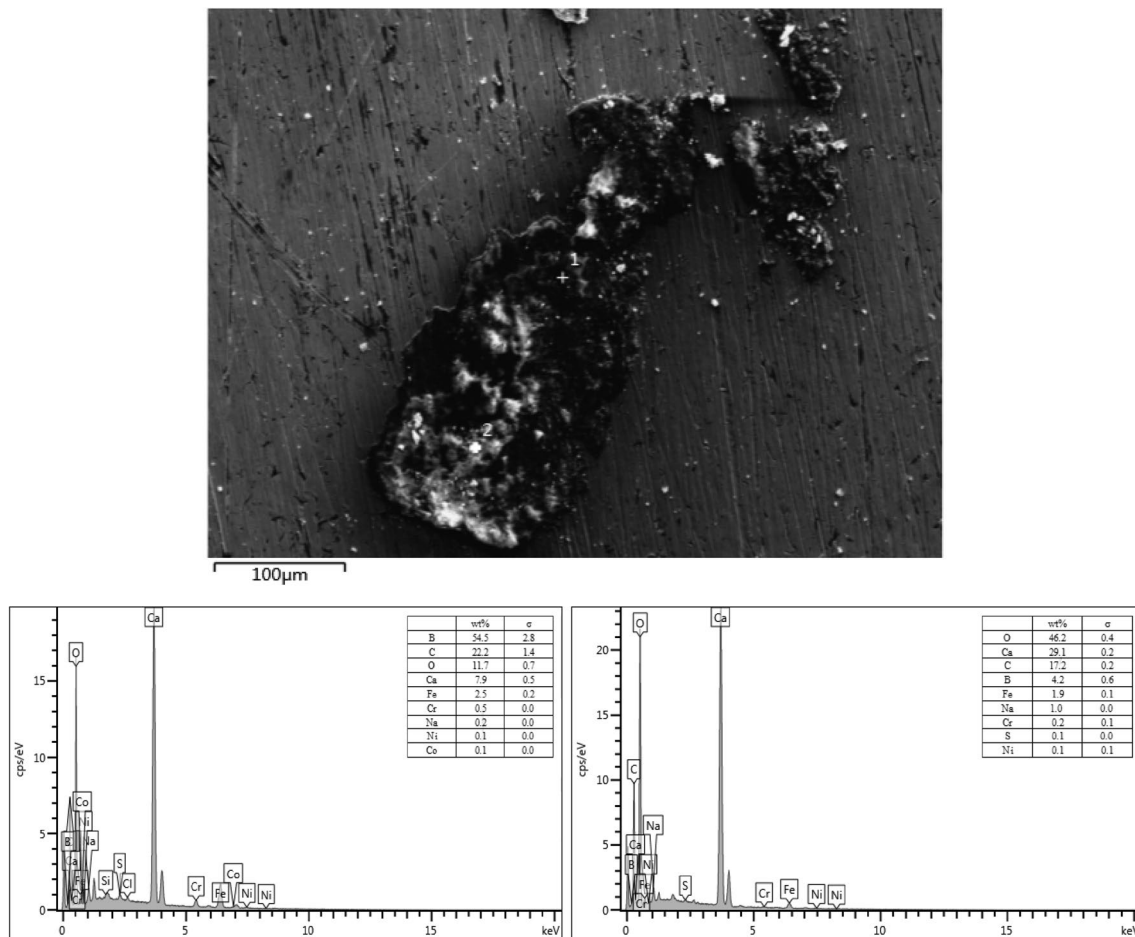


Fig. 22 SEM and EDS of corrosion products of Fe–15Mo cladding coating

austenite phase area, making the  $\sigma$  phase significantly lower, thus improving the corrosion resistance.

## 4 Conclusions

1. Fe–Mo coatings with different Mo were prepared on 65Mn matrix by synchronous powder feeding laser. It was found that the microstructure of the coating is dense, with no obvious holes or cracks on the surface, and shows a good metallurgical bonding. The composition distribution of Fe–Mo coatings is uniform, Mo and Cr segregates at grain boundary, forming eutectic products, which play a role in fine grain strengthening and dispersion strengthening.
2. The Fe–Mo coatings substantially improve wear resistance with a slight reduction in impact toughness. Mo can improve the toughness of the coating to some extent. At the same time, Ni and Co can significantly reduce the formation tendency of  $\sigma$  phase, which make the coating have higher hardness and greater impact toughness.
3. The hardness of Fe–Mo coating is nearly 2 times higher than that of 65Mn matrix. The impact abrasive wear rate and the erosion abrasive wear rate are reduced by 1 times compared to the 65Mn matrix. The hardness and wear resistance of the coating have been significantly improved. The Fe–Mo coating has a much higher corrosion resistance than the 65Mn matrix, and the Fe–15Mo coating has the best corrosion resistance.

**Funding** This work is supported by The National Natural Science Foundation of China (51575234, 51872122), The Postdoctoral Science Foundation of China (2017M620286), The Key Research and Development Program of Shandong Province, China (2018CXGC0809), Major basic research projects of Shandong Natural Science Foundation (ZR2020ZD06), Project of Shandong Province Higher Educational Youth Innovation Science and Technology Program (2019KJB021), and Taishan Scholars and Youth Innovation in Science and Technology Support Plan of Shandong Province University.



## References

- J. Singh, S.S. Chatha, B.S. Sidhu, Abrasive wear characteristics and microstructure of Fe-based overlaid ploughshares in different field conditions. *Soil Tillage Res.* **205**, 104771 (2021). <https://doi.org/10.1016/j.still.2020.104771>
- A. Kalácska, P.D. Baets, D. Fauconnier, F. Schramm, L. Freichs, J. Sukumaran, Abrasive wear behaviour of 27MnB5 steel used in agricultural tines. *Wear* **442–443**, 203107 (2020). <https://doi.org/10.1016/j.wear.2019.203107>
- B. Wei, L. Yan, L.Z. Jiang, Z.L. Hu, S.S. Li, Errors of structural seismic responses caused by frequency filtering based on seismic wave synthesis. *Soil Dyn. Earthq. Eng.* **149**, 10862 (2021). <https://doi.org/10.1016/j.soildyn.2021.106862>
- P. Li, D. Liu, W. Bao, L. Ma, Y. Duan, Surface characterization and diffusion model of pack borided TB2 titanium alloy. *Ceram. Int.* **44**, 18429–18437 (2018). <https://doi.org/10.1016/j.ceramint.2018.07.060>
- K.Y. Chen, X.F. Yang, Y.F. Zhang, H. Yang, G.J. Lv, Y.L. Gao, Research progress of improving surface friction properties by surface texture technology. *Int. J. Adv. Manuf. Technol.* **116**, 2797–2821 (2021). <https://doi.org/10.1007/s00170-021-07614-1>
- X.Y. Wang, D.Y. Qu, Y.H. Duan, M.J. Peng, Wear and corrosion properties of a B–Al composite layer on pure titanium. *Ceram. Int.* **48**, 12038–12047 (2022). <https://doi.org/10.1016/j.ceramint.2022.01.061>
- Y.H. Duan, X.Y. Wang, D. Liu, W.Z. Bao, P. Li, M.J. Peng, Characteristics, wear and corrosion properties of borided pure titanium by pack boriding near  $\alpha \rightarrow \beta$  phase transition temperature. *Ceram. Int.* **46**, 16380–16387 (2020). <https://doi.org/10.1016/j.ceramint.2020.03.197>
- D.Y. Qu, D. Liu, X.Y. Wang, Y.H. Duan, M.J. Peng, Corrosion and wear properties of TB2 titanium alloy borided by pack boriding with  $\text{La}_2\text{O}_3$ . *Trans. Nonferrous Metals Soc. China* **32**, 868–881 (2022). [https://doi.org/10.1016/S1003-6326\(22\)65839-4](https://doi.org/10.1016/S1003-6326(22)65839-4)
- M. Keddam, M. Ortiz-Dominguez, M. Elias-Espinosa, A.A. Flores, J.Z. Silva, D.Z. Zepeda, O.A.G. Vargas, Kinetic investigation and wear properties of  $\text{Fe}_2\text{B}$  layers on AISI 12L14 steel. *Metall. Mater. Trans. A* **49**, 1895–1907 (2018). <https://doi.org/10.1007/s11661-018-4535-1>
- D. Liu, Y.H. Duan, W.Z. Bao, M.J. Peng, Characterization and growth kinetics of boride layers on Ti–5Mo–5V–8Cr–3Al alloy by pack boriding with  $\text{CeO}_2$ . *Mater. Charact.* **164**, 110362 (2020). <https://doi.org/10.1016/j.matchar.2020.110362>
- Y.H. Duan, P. Li, Z.Z. Chen, J. Shi, L.S. Ma, Surface evolution and growth kinetics of Ti6Al4V alloy in pack boriding. *J. Alloy. Compd.* **742**, 690–701 (2018). <https://doi.org/10.1016/j.jallcom.2018.01.383>
- L.F. Hu, J. Li, Y.H. Lv, Y.F. Tao, Corrosion behavior of laser-clad coatings fabricated on Ti6Al4V with different contents of TaC addition. *Rare Met.* **39**, 436–447 (2020). <https://doi.org/10.1007/s12598-017-0973-y>
- J.B. Cheng, B. Sun, Y.Y. Ge, X.L. Hu, L.H. Zhang, X.B. Liang, X.C. Zhang, Nb doping in laser-clad  $\text{Fe}_{25}\text{Co}_{25}\text{Ni}_{25}(\text{B}_{0.7}\text{Si}_{0.3})_{25}$  high entropy alloy coatings: microstructure evolution and wear behavior. *Surf. Coat. Technol.* **402**, 126321 (2020). <https://doi.org/10.1016/j.surfcoat.2020.126321>
- X. Wen, X.F. Cui, G. Jin, X.R. Zhang, Y. Zhang, D. Zhang, Y.C. Fang, Design and characterization of  $\text{FeCrCoAlMn}_{0.5}\text{Mo}_{0.1}$  high-entropy alloy coating by ultrasonic assisted laser cladding. *J. Alloys Compd.* **835**, 155449 (2020). <https://doi.org/10.1016/j.jallcom.2020.155449>
- S.R. More, D.V. Bhatt, J.V. Menghani, Resent research status on laser cladding as erosion resistance technique—an overview. *Mater. Today* **4**, 9902–9908 (2017). <https://doi.org/10.1016/j.matpr.2017.06.291>
- Y.Z. Li, Y. Shi, E. Olugbade, Microstructure, mechanical, and corrosion resistance properties of  $\text{Al}_{0.8}\text{CrFeCoNiCu}_x$  high-entropy alloy coatings on aluminum by laser cladding. *Mater. Res. Express.* **7**, 026504 (2020). <https://doi.org/10.1088/2053-1591/ab6c9b>
- S.D. Sun, D. Fabijanic, C. Barr, Q.C. Liu, K. Walker, N. Matthews, N. Orchowski, M. Easton, M. Brandt, In-situ quench and tempering for microstructure control and enhanced mechanical properties of laser clad AISI 420 stainless steel powder on 300M steel substrates. *Surf. Coat. Technol.* **333**, 210–219 (2018). <https://doi.org/10.1016/j.surfcoat.2017.10.080>
- Y. Yang, A.H. Wang, D.H. Xiong, Z.W. Wang, D. Zhou, S.Q. Li, H. Zhang, Effect of Cr content on microstructure and oxidation resistance of laser-clad Cu–Ni–Fe–Mo–xCr alloy coating. *Surf. Coat. Technol.* **384**, 125316 (2020). <https://doi.org/10.1016/j.surfcoat.2019.125316>
- F.Z. Dai, Y.J. Sun, Y.X. Ren, H.M. Xiang, Y.C. Zhou, Segregation of solute atoms in ZrC grain boundaries and their effects on grain boundary strengths. *J. Mater. Sci. Technol.* **101**, 234–241 (2022). <https://doi.org/10.1016/j.jmst.2021.05.058>
- C.M. Lin, W.Y. Kai, C.Y. Su, K.H. Key, Empirical alloys-by-design theory calculations to the microstructure evolution mechanical properties of Mo-doped laser cladding NiAl composite coatings on medium carbon steel substrates. *J. Alloys Compd.* **702**, 679–686 (2017). <https://doi.org/10.1016/j.jallcom.2017.01.278>
- C.Y. Liu, P. Xu, D.Y. Zheng, Q.B. Liu, Study on microstructure and properties of a Fe-based SMA/PZT composite coating produced by laser cladding. *J. Alloys Compd.* **831**, 154813 (2020). <https://doi.org/10.1016/j.jallcom.2020.154813>
- Z. Gu, P. Mao, Y.F. Gou, Y. Chao, S.Q. Xi, Microstructure and properties of  $\text{MgMoNbFeTi}_2\text{Y}_x$  high entropy alloy coatings by laser cladding. *Surf. Coat. Technol.* **402**, 126303 (2020). <https://doi.org/10.1016/j.surfcoat.2020.126303>
- J. Liu, Y. Chen, J. Zhang, Oxidation behavior of Ni–Mo–Si alloy coatings fabricated on carbon steel by laser cladding. *Surf. Coat. Technol.* **375**, 903–910 (2019). <https://doi.org/10.1016/j.surfcoat.2019.08.001>
- H.S. Maharana, K. Mondal, Manifestation of Hall–Petch breakdown in nanocrystalline electrodeposited Ni–MoS<sub>2</sub> coating and its structure dependent wear resistance behavior. *Surf. Coat. Technol.* **410**, 126950 (2021). <https://doi.org/10.1016/j.surfcoat.2021.126950>
- G.F. Chi, D.Q. Yi, B. Jiang, L.Y. Yang, H.Q. Liu, Crack propagation during Charpy impact toughness testing of Ti–Al–V–Mo–Zr alloy tubes containing equiaxed and lamellar microstructures. *J. Alloys Compd.* **852**, 156581 (2020). <https://doi.org/10.1016/j.jallcom.2020.156581>
- C. Sun, P.X. Fu, X.P. Ma, H.H. Liu, N.Y. Du, Y.F. Cao, H.W. Liu, D.Z. Li, Effect of matrix carbon content and lath martensite microstructures on the tempered precipitates and impact toughness of a medium-carbon low-alloy steel. *J. Mater. Res. Technol.* **9**, 7701–7710 (2020). <https://doi.org/10.1016/j.jmrt.2020.05.002>
- Y.A.H. Jose, V.U. Alejandro, P.G. Katherine, P.H. Rodrigo, J.T. Maria, M.A. Jose, Boron addition in a non-equiatom  $\text{Fe}_{30}\text{Mn}_{30}\text{Co}_{10}\text{Cr}_{10}$  alloy manufactured by laser cladding: microstructure and wear abrasive resistance. *Appl. Surf. Sci.* **515**, 146084 (2020). <https://doi.org/10.1016/j.apsusc.2020.146084>
- Q. Shao, Continuum model of abrasive layer in an abrasive wear test. *Wear* **259**, 36–43 (2005). <https://doi.org/10.1016/j.wear.2005.03.015>
- F. Ficici, The experimental optimization of abrasive wear resistance model for an in-situ  $\text{AlB}_2/\text{Al–4Cu}$  metal matrix composite.

- Ind. Lubr. Tribol. **68**, 632–639 (2016). <https://doi.org/10.1108/ILT-12-2015-0198>
30. G. Saha, K. Valtonen, A. Saastamoinen, P. Peura, V.T. Kuokkala, Impact-abrasive and abrasive wear behavior of low carbon steels with a range of hardness-toughness properties. *Wear* **450–451**, 203263 (2020). <https://doi.org/10.1016/j.wear.2020.203263>
  31. E.D. Wen, R.B. Song, C.H. Cai, Study of the three-body impact abrasive wear behaviour of a low alloy steel reinforced with niobium. *J. Manuf. Process.* **46**, 185–193 (2019). <https://doi.org/10.1016/j.jmapro.2019.08.026>
  32. I. Fordyce, M. Annasamy, S.D. Sun, D. Fabijanic, S.C. Gallo, M. Leary, M. Easton, M. Brandt, The effect of heat treatment on the abrasive and erosive wear behaviour of laser metal deposited Fe–28Cr–2.7C alloy. *Wear* **458–459**, 203410 (2020). <https://doi.org/10.1016/j.wear.2020.203410>
  33. F. Cucinotta, L. Scappaticci, F. Sfravara, F. Morelli, F. Mariani, M. Varani, M. Mattetti, On the morphology of the abrasive wear on ploughshares by means of 3D scanning. *Biosyst. Eng.* **179**, 117–125 (2019). <https://doi.org/10.1016/j.biosystemseng.2019.01.006>
  34. S. Natarajan, E.E. Anand, K.S. Akhilesh, A. Rajagopal, P.P. Nambiar, Effect of graphite addition on the microstructure, hardness and abrasive wear behavior of plasma sprayed NiCrBSi coatings. *Mater. Chem. Phys.* **175**, 100–106 (2016). <https://doi.org/10.1016/j.matchemphys.2016.02.076>
  35. R. Lal, D.C. Reicosky, J.D. Hanson, Evolution of the plow over 10,000 years and the rationale for no-till farming. *Soil Till. Res.* **93**, 1–12 (2007). <https://doi.org/10.1016/j.still.2006.11.004>
  36. J.L. Zhou, D.J. Kong, Immersion corrosion and electrochemical performances of laser cladded FeSiB, FeSiBCr and FeSiBCrMo coatings in 3.5 wt% NaCl solution, *Surf. Coat. Technol.* **383**, 125229 (2020). <https://doi.org/10.1016/j.surfcoat.2019.125229>
  37. X. Xu, H.F. Lu, K.Y. Luo, J.H. Yao, L.Z. Xu, J.Z. Lu, Y.F. Lu, Mechanical properties and electrochemical corrosion resistance of multilayer laser cladded Fe-based composite coatings on 4Cr5MoSiV1 steel. *J. Mater. Process. Technol.* **284**, 116736 (2020). <https://doi.org/10.1016/j.jmatprotec.2020.116736>

**Publisher's Note** Springer Nature remains neutral with regard to jurisdictional claims in published maps and institutional affiliations.

Springer Nature or its licensor holds exclusive rights to this article under a publishing agreement with the author(s) or other rightsholder(s); author self-archiving of the accepted manuscript version of this article is solely governed by the terms of such publishing agreement and applicable law.